Rational Design and Nanoscale Integration of Multi-Heterostructures as Highly Efficient Photocatalysts

Final Technical Report

Period covered by the report: (07/01/12-06/30/17)

Xiangfeng Duan

University of California, Los Angeles

PREPARED FOR THE U.S. DEPARTMENT OF ENERGY OFFICE OF BASIC ENERGY SCIENCES, DIVISION OF MATERIALS SCIENCE AND ENGINEERING UNDER CONTRACT NO. DE-SC0008055.

Abstract

The central goal of this project is to design and synthesize complex multi-hetero-nanostructures and fundamental investigation of their potential as efficient and robust photocatalysts. Specifically, the project aims to develop a nanoscale light-harvesting antenna that can efficiently convert solar photon energy into excited electrons and holes, and integrate such antenna with efficient redox nanocatalysts that can harness the photo-generated carriers for productive electrochemical processes. Focusing on this central goal, we have investigated several potential light-harvesting antennas including: silicon nanowires, nitrogen-doped TiO_2 nanowires and the emerging perovskite materials. We also devoted considerable effort in developing electrocatalysts including: hydrogen evolution reaction (HER) catalysts, oxygen evolution reaction (OER) catalysts and oxygen reduction reaction (ORR) catalysts. In previous annual reports, we have described our effort in the synthesis and photoelectrochemical properties of silicon, TiO_2, perovskite-based materials and heterostructures. Here, we focus our discussion on the recent effort in investigating charge transport dynamics in organolead halide perovskites, as well as carbon nanostructure and platinum nanostructure-based electrocatalysts for energy conversion and storage.

1. Study on electronic and ionic transport dynamics in organolead halide perovskites as light harvesters

Ion migration has been postulated as the underlying mechanism responsible for the hysteresis in organolead halide perovskite devices. However, the electronic and ionic transport dynamics and how they impact each other in organolead halide perovskites remain elusive to date. We conducted a systematic investigation of the electronic and ionic transport dynamics in organolead halide perovskite microplate crystals and thin films using temperature-dependent transient response measurements. Our study reveals that thermally activated ionic and electronic conduction coexists in perovskite devices. The extracted activation energies suggest that the electronic transport is easier, but ions migration is harder in microplates than in thin films, demonstrating that the crystalline quality and grain boundaries can fundamentally modify electronic and ionic transport in perovskites. These findings offer valuable insight on the electronic and ionic transport dynamics in organolead halide perovskites, which is critical for optimizing perovskite devices with reduced hysteresis and improved stability and efficiency.

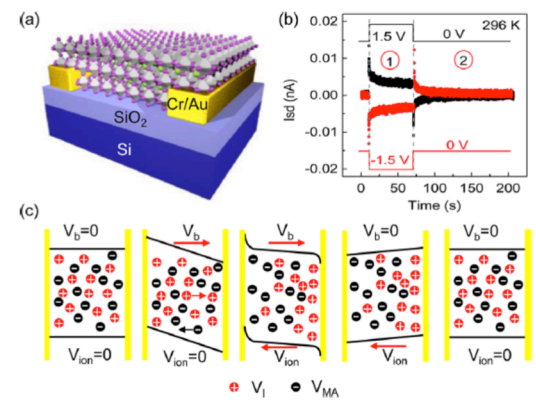

Fig. 1. Temporal response and schematics of the ion migration in organolead halide perovskite. (a) Schematic of a two-probe halide perovskite film device. (b) Temporal response curves. Stage 1: the external bias is applied, and stage 2: the external bias is removed. (c) Schematic diagrams indicating the dynamics of ionic transport following external bias. The two yellow bars represent Cr/Au electrodes, and organolead halide perovskite film fills between these two electrodes.

The two-probe symmetric Cr/Au (5 nm/50 nm) electrodes (Fig. 1a) are utilized. The perovskite thin film was spin-casted on 300 nm SiO_2/Si substrate with pre-fabricated electrodes, following similar protocols developed previously. For the individual perovskite microplate devices, we adopted the pattern growth method to directly grow the microplates across the pre-defined electrode pairs. Fig. 1b shows the switchable behavior attributed to ion migration in perovskites. Dynamics of ion migration is described in Fig. 1c. First, without the external bias, V_I, V_{Pb}, and V_{MA} are randomly distributed throughout the device channel. With the application of a

positive bias (pointing from left to right in Fig. 1c), the electronic current is instantly observed due to a much faster speed of electrons/holes compared with that of ions. Then, the ions start to drift under the applied external bias, leading to an ionic current with the same polarity as that of the electronic current. With continued external bias, the oppositely charged ions pile up near to the perovskite−electrode interfaces, resulting in an ion-induced electric field with the direction opposite to the external electric field, which partially cancels the external bias and reduces the electronic current. As ions progressively move toward and accumulate near the perovskite−electrode interfaces, the ion-induced electric field continuously increases, leading to a gradual decrease of total current, and finally to a stable value when the ion accumulation reaches the equilibrium conditions (stage 1 in Fig. 1b)

To quantitatively characterize the contributions from electronic transport and ionic conduction, and determine the magnitude of the ion-induced electric potential in our devices, we investigated the temporal response of the current curve when an increasing external bias is applied (stage 1) and removed (stage 2), and fit both of them with a bi-exponential function. As a result, necessary parameters were extracted for further determining the current origins and magnitude of the ion-induced electric field.

Fig. 2a displays the temporal response of current curves of a thin-film perovskite device upon the application and removal of a positive (black) or negative (red) bias voltage, along with the corresponding bias sequences. Fig. 2b,c shows temporal response curves at stages 1 and 2, with varying external bias. Parameters from the fitting of curves show how ion-induced electric field first increases with the external bias and then saturates. The saturation of the ion-induced electric field is perhaps due to the lack of available mobile vacancies. Based on the continuum theory developed in ionic liquids, we have studied the evolution of the distribution of the ions under the applied bias with time. The calculations indicate that the positive ions pile up near the cathode, while net negative charges accumulate around the anode when the equilibrium conditions have established. With increasing time, ions progressively accumulate near the perovskite−electrode interfaces, and the distribution of iodine vacancies gradually decays into the channel, possibly due to the expelling of positive ions by the pre-accumulated positive ions near the cathode interface. The accumulated ions could generate an opposite polarity electric field to the applied bias and drive the current to flow after removing the applied bias, which is consistent with the experimental results.

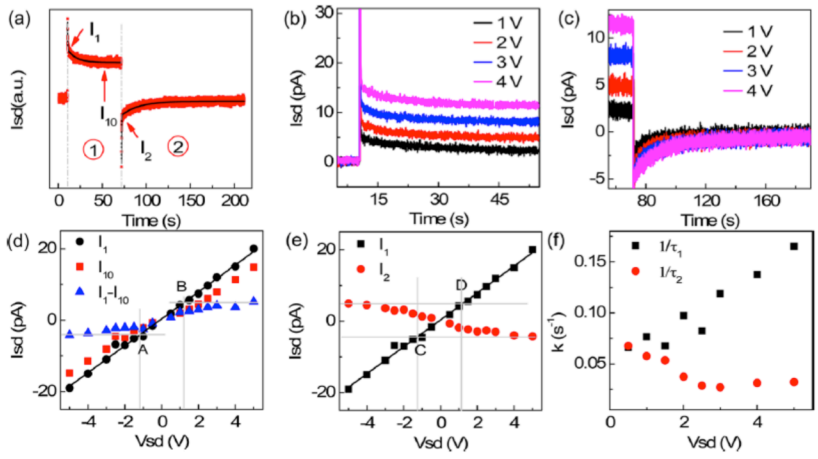

Fig. 2. External bias-dependent temporal response in organolead halide perovskite. (a) Temporal response. (b, c) The applied external bias dependence of temporal response curves for stage1 (b) and stage 2 (c) for the organolead halide perovskite film device in the dark. (d) The applied external bias dependence. The solid black line is the linear fitting result. (e) The applied external bias dependence of I_1 and I_2 extracted from (b) and (c). The solid black line is linear fitting result. (f) The applied external bias dependence of ion decay rate extracted from (b) and (c).

To further explore the nature of electronic and ionic transport, we measured temporal response under different temperatures (Fig. 3a,b). Fig. 3c shows the electronic transport is thermally activated. The activation energies derived from I_1 and I_2 are estimated to be 360 and 540 meV, respectively. The larger activation energy for I_2 can be partly attributed to the smaller ion-induced electric field at lower temperatures. Electronic current I_2 is driven by ion-induced electric field. The decrease of ion-induced electric potential due to the slower ion migration rate at low temperature could lead to an overestimation of the activation energy extracted from I_2.

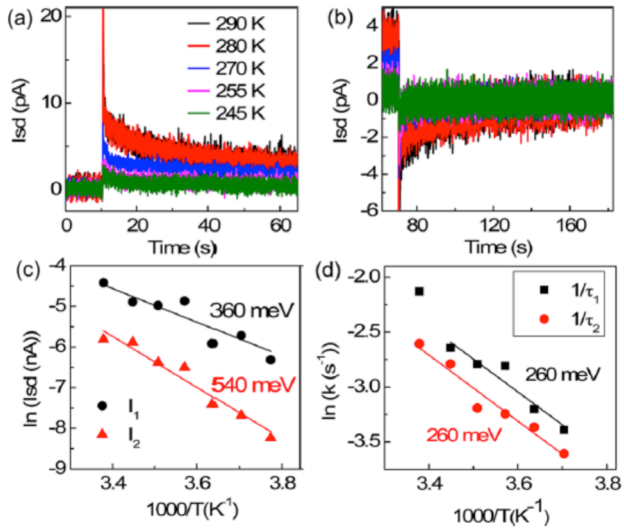

Fig. 3. Temperature-dependent temporal response in organolead halide perovskite. (a, b) The temperature dependence of temporal response curves for stages 1 (a) and 2 (b) under an applied external bias of 3 V for the organolead halide perovskite film device in the dark. (c) Arrhenius plots of the temperature dependence of I1 and I2 extracted from (a) and (b). (d) Arrhenius plots of the temperature dependence of ion decay rate extracted from (a) and (b).

The migration of ions is expected to be affected by the perovskite grain size since devices with a larger perovskite grain size have a smaller number of grain boundaries and lower vacancy concentration. To further probe how the grain size and grain boundary impact the electronic and ionic transport, we also studied microplate devices with higher crystalline quality and fewer grain boundaries (Fig. 4). The polycrystalline thin-film devices are obtained through a conventional spin-coating process with grain size typically on the order of 10 nm and abundant grain boundaries; whereas, the nearly single-crystalline microplate devices are obtained using a vapor phase intercalation approach with much larger grain sizes (micrometer scale) and few grain boundaries. The thicknesses of both the thin films and microplates are around 150 nm. Notably, our study reveals that both the ion motion

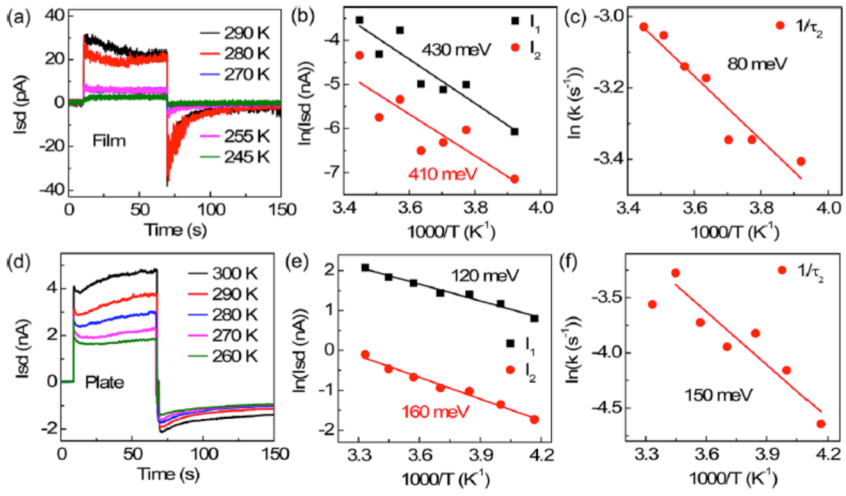

Fig. 4. Comparisons of temperature-dependent temporal response in organolead halide perovskite film and microplate devices under illumination. (a) The temperature dependence of temporal response curves. (b) Arrhenius plot of the temperature dependence of I_1 and I_2. (c) Arrhenius plot of the temperature dependence of ion decay rate extracted from (a). (d) The temperature dependence of temporal response. (e) Arrhenius plot of the temperature dependence of I_1 and I_2 extracted from (d). The solid lines are linear fitting results. (f) Arrhenius plot of the temperature dependence of ion decay rate extracted from (d). The solid line is linear fitting result.

and hysteresis can be greatly suppressed or eliminated in nearly single crystalline microplates due to greatly reduced grain boundaries and better crystalline quality. The extracted activation energy for electronic transport in microplates (70 meV) is much smaller than that in thin films (430 meV), while the activation energy for ionic transport in microplates (210 meV) is considerably larger than that in thin films (90 meV). The electronic transport activation energy and ionic transport activation energy have been derived from the dynamics measurements and summarized in Table 1.

In essence, we have investigated the electronic and ionic transport dynamics in organolead halide perovskite thin films and microplates. Our studies reveal that both the electronic and ionic transport processes are thermally activated with the derived activation energies in agreement with that of migration of iodine ions reported in other halide perovskites. Our study evidently demonstrates that the ion migration and hysteresis in current−voltage curves in organolead halide perovskite are highly dependent on the crystalline quality, and could be greatly suppressed or completely removed in nearly single crystalline microplate devices. These findings will motivate further efforts to probe and control the ionic transport dynamics in organolead halide perovskite materials and offer significant insight for optimizing and designing new solar cell device architectures with improved efficiencies and stability. In particular, with continued effort in the synthesis of perovskite crystals with improved crystalline quality, even smaller or negligible hysteresis may be expected.

Table 1. Summary of Activation Energies and Ion-Induced Electric Potential Across the Device Channel for Both Perovskite Film and Microplate Devices in the Dark Under Stage 2 Illumination and Full Illumination

	electronic transport activation energy		ionic transport activation energy		
	from I_1 (meV)	from I_2 (meV)	from τ_1 (meV)	from τ_2 (meV)	ion-induced potential (V)
film (dark)	360 ± 50	540 ± 40	260 ± 40	260 ± 30	1.2
film (light @ stage 2)	–	**430 ± 50**	–	**90 ± 10**	–
film (light @ stages 1 and 2)	430 ± 80	410 ± 100	–	80 ± 10	0.9
plate (dark)	–	–	–	–	–
plate (light @ stage 2)	–	**70 ± 10**	–	**210 ± 20**	–
plate (light @ stages 1 and 2)	120 ± 10	160 ± 10	–	150 ± 25	0.3

2. Study on the effect of thermal annealing on charge transport

To date, charge transport parameters of perovskite materials are mainly derived from the study of photovoltaic devices, while the investigation on perovskite field-effect transistors (FETs) is still in its infancy stage, largely limited to spin-coated perovskite thin films due to the solubility of organolead halide perovskite materials in many common solvents (e.g., water, acetone and isopropanol) and instability under ambient conditions. All of those factors prevent the adoption of conventional lithography techniques to directly fabricate functional devices based on these perovskite materials. To this end, we have fabricated FET from the individual methylammonium lead triiodide perovskite $MAPbI_3$ microplate by adopting a two-step growth method we developed and a dry-transfer technique, and conducted a systematical investigation of the effects of thermal annealing on the charge transport properties. The result shows that moderate thermal annealing process can convert the $MAPbI_3$ from *n*-type to *p*-type behavior, and significantly reduce the field-effect mobility without noticeable change in crystal structure or the photoluminescence (PL) spectra, indicating that the charge transport measurement provides a more sensitive way to probe the low concentration defects in organolead halide perovskite materials.

Figures 5a, and 5b show the schematic of a two-terminal graphene-contacted FET without BN encapsulation and the corresponding optical image. The output characteristics (Fig. 5c) indicate an *n*-type semiconductor behavior, which is also confirmed by the transfer characteristics (Fig. 5d). A considerable hysteresis has been observed for all transfer curves at

77 K and higher temperatures (Fig. 5e). The mobility versus temperature (Fig. 5f) shows the field effect electron mobility is about 4 $cm^2 \cdot V^{-1} \cdot s^{-1}$ at 77 K, continuously decreasing with increasing temperature from 77 K to 120 K. A sudden increase around 120 K-140 K appears due to the orthorhombic to a tetragonal phase transition.

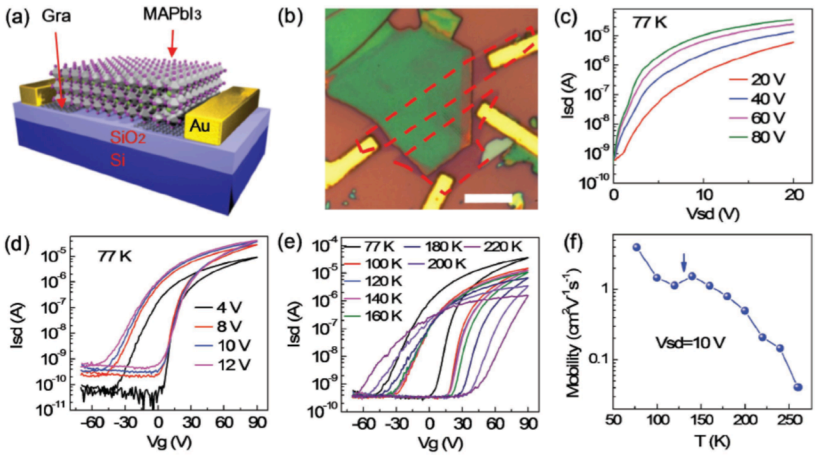

Fig. 5. (a) Schematic of the halide perovskite microplate field-effect transistor. (b) The optical image of a bilayer graphene-contacted device. The red dashed lines indicate graphene contacts.The thickness of the microplate is around 40 nm and the scale bar is 8 μm. (c) Output and (d) transfer characteristics of the graphene contact field-effect transistor at 77 K. (e) The temperature dependent transfer characteristics of the graphene-contacted field-effect transistor. (f) The temperature dependent field-effect electron mobility measured with a source–drain voltage of 10 V extracted from (e), the blue arrow indicates the tetragonal-to-orthorhombic phase transition temperature.

We have further encapsulated the $MAPbI_3$ with BN to present degradation (Fig. 6a,b). The source-drain current increases with the increasing positive back-gate voltage, indicating the *n*-type semiconductor behavior (Fig. 6c). The transfer characteristics show that the BN covered $MAPbI_3$ FET still exhibits dominant *n*-type behavior at 77 K (Fig. 6d). A noticeable *p*-type semiconductor behavior has also been observed in transfer characteristics, revealing that the BN covered $MAPbI_3$ FET changes from a unipolar *n*-type in $MAPbI_3$ FET to an ambipolar behavior. As the temperature increases, the *p*-type behavior gradually diminishes and finally vanishes around 180 K (Fig. 6e). The field-effect electron mobility first increases and reaches a maximum value of 3 $cm^2 \cdot V^{-1} \cdot s^{-1}$ around 160 K and then decreases above 180 K with increasing temperature (Fig. 6f). The trend of field-effect electron mobility versus temperature is strikingly different from what is observed in the uncovered $MAPbI_3$ FET shown previously, which may be due to the presence of noticeable *p*-type behavior at low temperatures. The presence of the *p*-type behavior indicates that the Fermi level moves toward valence. As a result, the barrier between the $MAPbI_3$ microplate and graphene for electrons increases, leading to a smaller field-effect electron mobility at a lower temperature. As the temperature increases, the *p*-type behavior continuously reduces, implying the Fermi level shifts toward the conduction band again. Consequently, the barrier for electrons reduces, leading to an increase of the field-effect electron mobility. Above 180 K, the *p*-type behavior completely vanishes, thus a decrease of mobility with temperature is due to the increasing electron-phonon scattering.

Encapsulating the $MAPbI_3$ microplate FET by BN involves a thermal annealing step (90 °C for 3 min) during the dry transfer of BN. This thermal annealing step plays a substantial role in the conversion of the unipolar *n*-type semiconductor behavior to the ambipolar behavior. Since the annealing temperature (90 °C) is lower than the drying temperature for spin-coated perovskite thin films (100 °C), we do not expect that this annealing temperature can introduce a lot of defect states. To further probe the thermal annealing effect induced transition, we annealed BN covered $MAPbI_3$ FET at 120 °C for 3 min in the ambient condition; we expect to observe more obvious change of electrical properties. With this additional annealing, the source-drain current increases as the gate voltage decreases from positive to negative, indicating a *p*-type behavior as well. The device transition from *n*-type dominant to *p*-type

dominant behavior is further demonstrated. Meanwhile, the hysteresis significantly increases and the source-drain current decreases by more than one order of magnitude.

Based on above discussions, thermal annealing can induce three effects: (1) change from unipolar *n*-type behavior to ambipolar behavior, and finally to unipolar p-type behavior; (2) the source-drain current significantly reduces with the thermal annealing; (3) the trend of field-effect mobility versus temperature for ambipolar FET is strikingly different from that of both unipolar *n*-type and *p*-type behavior. Since the BN layer is rather inert and the $MAPbI_3$ microplate is around 150 nm in thickness for the BN covered device, it is not expected that the BN layer can introduce the doping effect to the bottom part of the $MAPbI_3$ microplate; thus, changing the microplate from unipolar *n*-type to ambipolar and eventually to unipolar *p*-type behavior. It has been shown previously that the thermal annealing can lead to the degradation of the performance of $MAPbI_3$ thin film solar cells even with the annealing temperature as low as 85 °C in the inert atmosphere, which was attributed to the low formation energy of $MAPbI_3$. One possibility for the observed phenomena is that the formation of Pb clusters might induce the *p*-type doping. Hence, the $MAPbI_3$ FET gradually transits from unipolar *n*-type to ambipolar and finally to unipolar *p*-type with increasing annealing temperature and annealing time. Furthermore, the disintegration of $MAPbI_3$ and formation of the Pb clusters would increase the carrier-defect scattering, leading to the reduction of source-drain current and field-effect mobility.

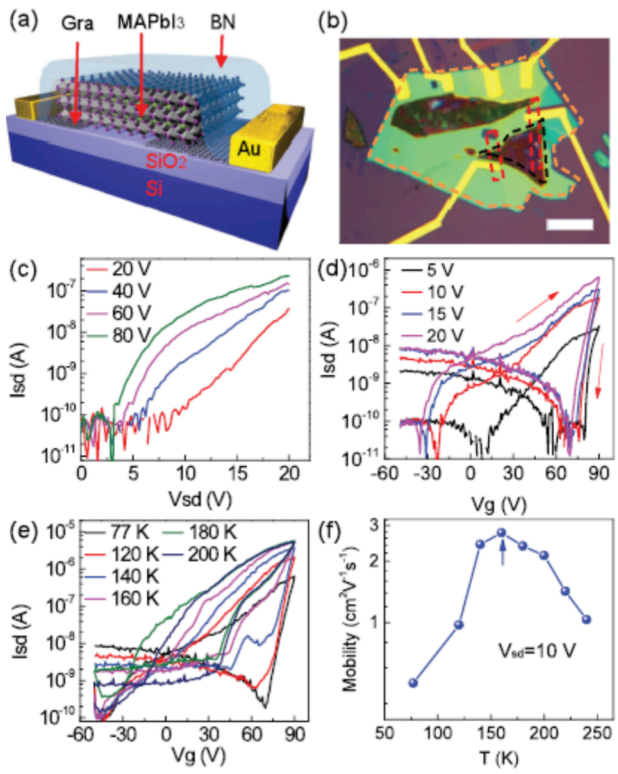

Fig. 6. (a) Schematic of halide perovskite microplate field-effect transistor fabricated on a 300 nm SiO_2/Si substrate with monolayer graphene as contact covered by a layer of BN. (b) The optical image of the BN covered device. (c) Output and (d) transfer characteristics of the BN covered field-effect transistor at 77 K. The device has been thermally annealed for 3 min at 90 °C during the BN transfer process. (e) The temperature dependent transfer characteristics of the BN covered field-effect transistor. (f) The temperature dependent electron field-effect mobility measured with a source-drain voltage of 10 V. The blue arrow indicates the tetragonal-to-orthorhombic phase transition temperature.

Additionally, after converting to *p*-type, the Fermi level of $MAPbI_3$ moves close to the valence band of $MAPbI_3$, resulting in a larger barrier between $MAPbI_3$ and graphene, which would increase contact resistance and thus decrease the source-drain current as well. Alternatively, the evolution of the electronic properties with annealing temperature may also be correlated with the PbI_2 back conversion.

In summary, we have investigated how thermal annealing influences the performance of $MAPbI_3$ microplate FETs. The thermal annealing process leads to a transition from unipolar *n*-type to ambipolar and finally to unipolar *p*-type behavior, which may be partially attributed the slight disintegration of $MAPbI_3$. Meanwhile, the source-drain current and mobility greatly decrease after thermal annealing due to enhanced carrier-defects scattering. We believe that

these findings will provide a better understanding of electrical properties of $MAPbI_3$ and shed light on the design and optimization of the electronic devices based on $MAPbI_3$. Due to the challenges in making reliable perovskite devices and the complications from various mobile ions, the charge transport in perovskite is significantly under-explored to date. Our BN encapsulated devices offer an interesting platform to probe the charge transport in these delicate perovskite materials. And our systematic investigations could inspire further efforts to understand the complicated charge transport characteristics in perovskite materials.

3. Fundamental investigation of gate-induced insulator to band-like transport transition in organolead halide perovskite

Understanding the intrinsic charge transport in organolead halide perovskites is essential for the development of high-efficiency photovoltaics and other optoelectronic devices. Despite the rapid advancement of the organolead halide perovskite in photovoltaic and optoelectronic applications, the intrinsic charge carrier transport in these materials remains elusive partly due to the difficulty of fabricating electrical devices and obtaining good electrical contact. We conducted systematic charge-transport studies on perovskite/graphene devices, revealing an insulator to band-like transport transition. This implies that the insulator to band-like transport transition depends on the orthorhombic-to-tetragonal phase-transition temperature and defect densities of the organolead halide perovskite microplates. Fig. 7a illustrates the schematic of a two-terminal organolead halide perovskite microplate FET with monolayer graphene contacts. Fig. 7b is the corresponding image. The output characteristics (I_{sd} vs V_{sd}) of the monolayer graphene-contacted organolead halide perovskite microplate FET at 77 K show that the source-drain current I_{sd} continuously increases with increasing positive gate voltage, indicating an *n*-type semiconductor behavior (Fig. 7c). The transfer characteristics also exhibit a unipolar *n*-type behavior for the monolayer graphene-contacted device (Fig. 7d). The electron field-effect mobility can be extracted from transfer characteristics (Fig. 7e). In general, the mobility continuously increases with the decrease in temperature but with a sudden fall around 170 K; it begins to increase again with further decreasing temperature below 170 K. The sudden fall of mobility around 170 K can be attributed to the tetragonal-to-orthorhombic phase transition, further confirmed by the temperature-dependent photoluminescence (PL) spectra (Fig. 7f). The presence of two emission peaks below 170 K is the evidence of the tetragonal inclusions within an orthorhombic phase (Fig. 7f); the lower energy emission peak originating from the tetragonal phase inclusions, and the orthorhombic phase leading to the higher energy emission peak. As

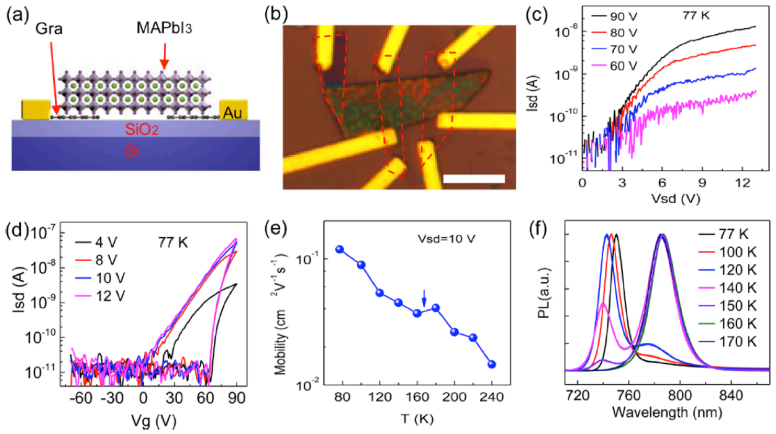

Fig. 7. (a) Schematic of the back-gate, back-contact halide perovskite microplate field-effect transistor fabricated on a 300 nm SiO_2/Si substrate with monolayer graphene stripes as contact. (b) Optical image of corresponding device. (c) Output and (d) transfer characteristics of the graphene contact field-effect transistor at 77 K. (e) Temperature-dependent field-effect. The blue arrow indicates the tetragonal-to-orthorhombic phase-transition temperature. (f) Temperature-dependent photoluminescence.

the temperature approaches to the phase-transition temperature (160 K−180 K), the portion of orthorhombic phase becomes negligibly small, leading to an unremarkable orthorhombic phase emission. While the increase in the mobility with the decreasing temperature above 170 K might be ascribed to the reduction of carrier−phonon interaction or due to large polaron transport that can be protected from scattering and trapping. The increase in mobility below 170 K is a result of reduction of electron−phonon interaction and the decrease in the small inclusions of tetragonal phase domains within orthorhombic phase.

To investigate how the tetragonal inclusion introduced disorders influences the charge transport, we display the temperature dependent transfer characteristics of a monolayer graphene contacted device below phase-transition temperature around 170 K (Fig. 8a). By varying temperature below 170 K, there is a source-drain current crossover for the positive sweeping near the gate voltage of 60 V. While the source-drain current increases with the decrease in temperature for the gate voltage larger than 60 V, a completely opposite trend of source-drain current was observed for the gate voltage smaller than 60 V (Fig. 8a). To demonstrate this trend more clearly, we extracted the source-drain current against temperature under different gate voltages, as shown in Fig. 8b. A clear insulator to band-like transport transition was seen with increasing gate voltage within the orthorhombic phase (< 180 K), whereas the source-drain current increases with decreasing temperature under all gate voltages investigated in tetragonal phase (> 180 K). When organolead halide perovskite is in the tetragonal phase above 180 K, the continuous increase in source-drain current with the decreasing temperature under all gate voltages within the tetragonal phase might be due to the fact that the charge carriers are protected as large polarons, which has been proposed previously and primarily supported by optical measurement. In contrast to the small polarons, where the thermally activated hopping dominates the charge transport, the large polarons with a large charge carrier effective mass can effectively reduce the carrier-phonon and carrier defect scattering, leading to the increase in the source-drain current with the decreasing temperature. Below 180 K within the orthorhombic phase, the small inclusions of tetragonal phase would introduce more grain boundaries and thus the in-gap electronic states (Fig. 8c). As a consequence, the Fermi level locates within the bandgap at low gate voltages due to a large amount of in-gap electronic states, leading to insulating behavior (Fig. 8c). As the gate voltage increases, all in-gap electronic states are filled, and the Fermi level shifts close to or into mobility edge, resulting in

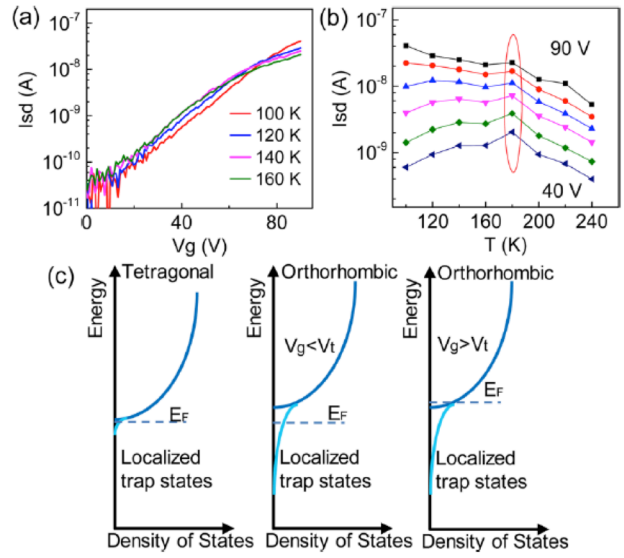

Fig. 8. (a) Temperature-dependent transfer characteristics. (b) Temperature-dependent source-drain current under different gate voltage. (c) Schematic diagrams of electronic structures for tetragonal phase (left panel) and orthorhombic phase under gate voltage smaller (middle panel) and larger (right panel) than the voltage (V_t) that the insulator to band-like transport transition occurs.

the band-like transport. Similar temperature-dependent behavior has been identified in polymers and organic semiconductors and can be attributed to variable range hopping transport with Coulomb interaction.

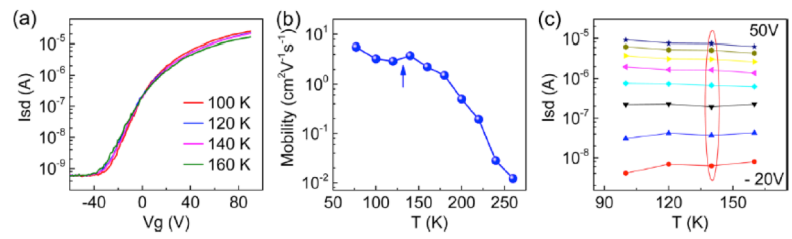

Fig. 9. (a) Temperature-dependent transfer characteristics. (b) Temperature-dependent field-effect mobility measured under a source-drain voltage of 10 V. The blue arrow indicates the tetragonal-to-orthorhombic phase transition temperature. (c) Temperature-dependent source-drain current under different gate voltages.

We carried out the same electrical measurement for a thinner organolead halide perovskite microplate transistor, which has a lower phase-transition temperature. The transfer characteristics of the monolayer graphene-contacted microplate device with a smaller thickness show the similar unipolar *n*-type behavior (Fig. 9a). A very similar mobility versus temperature behavior was observed for the thinner microplate devices. The temperature-dependent mobility curve indicates that the orthorhombic-to-tetragonal phase transition occurs at a lower temperature of ~ 130 K (Fig. 9b), consistent with previous temperature-dependent studies. The source-drain current versus temperature under different gate voltages shows that a similar insulator to band-like transport transition is present as well in the thinner microplate device right after the orthorhombic-to-tetragonal phase transition, demonstrating that this transition is due to the phase-transition-induced disorders (Fig. 9c). The observation of the insulator to band-like transport transition in our devices can be attributed to the better crystalline quality of our organolead halide microplates and graphene electrical contact. The intrinsic insulator to band-like transport transition is not smeared by the contact effect and can be observed here. In summary, we have observed the insulator to band-like transport transition induced by the gate voltage within the orthorhombic phase in organolead halide perovskite microplate devices with monolayer graphene as electrical contacts. This gate-induced insulator to band-like transport transition might be attributed to the disorders introduced by the tetragonal inclusions within the orthorhombic phase. Our findings are not only important to the fundamental research, but also have important practical implications in the development of the electronic and optoelectronic devices at low temperatures.

4. Tailoring the charge transport in three-dimensional structures for efficient energy storage

Nanostructured electrode materials have shown considerable promise for higher energy density and higher power density than conventional electrodes. However, these materials are usually limited to laboratory cells with ultrathin electrodes and very low mass loadings (< 1 $mg \cdot cm^{-2}$). To reach the requirements of commercial cells (mass loading of ~ 10 $mg \cdot cm^{-2}$ or more), sufficient charge must be delivered fairly rapidly across thick electrodes. This is especially challenging for emerging nanomaterials, which require more charge delivered in a given time than do conventional electrode materials. To realize the promise of the new electrode materials with intrinsically high capacity or high rate capability in practical devices, it is essential to develop new electrode architecture that can efficiently deliver sufficient electrons or ions to

make the full use of the electrode material at practical mass loading (*e.g.*, > 10 mg·cm^{-2}). Herein, we developed three-dimensional (3D) holey graphene frameworks to deliver promising charge transports for both electrons and ions (Fig. 10a-d). In general, the highly interconnected 3D graphene framework offers excellent electron transport, and the hierarchical porous structure ensures a high ion diffusion rate.

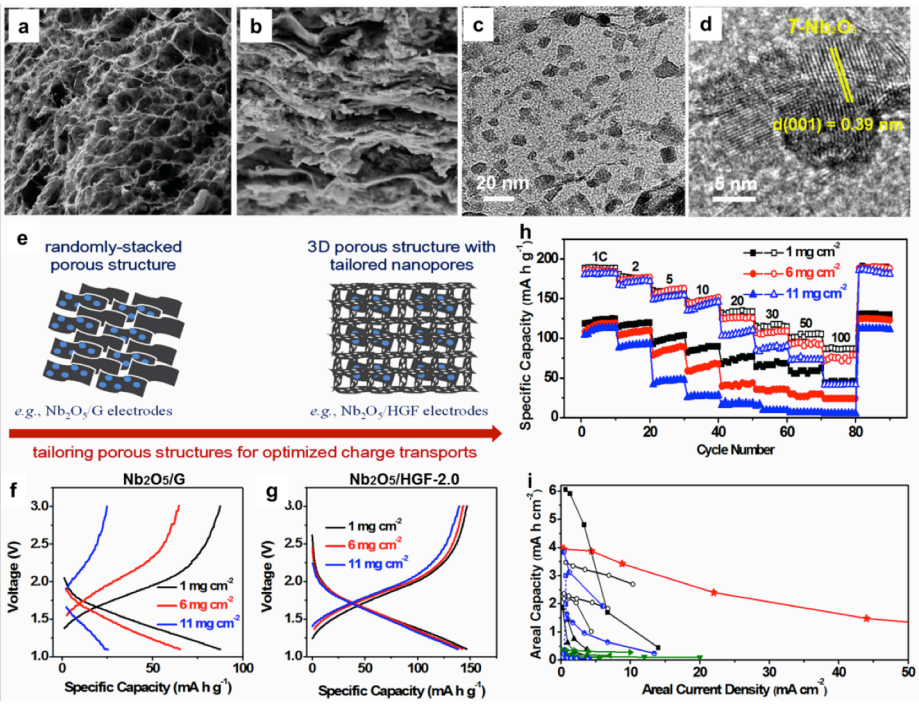

Fig. 10. Morphology of 3D composite electrodes (a) before and (b) after compression. (c) TEM image of graphene sheets with uniformly decorated *T*-Nb_2O_5 nanoparticles. (d) HR-TEM image of *T*-Nb_2O_5 nanoparticles. (e)The schematic of two different electrode structures for optimized charge transport. Galvanostatic charge-discharge curves for (f) Nb_2O_5/G control electrode and (g) Nb_2O_5/HGF-2.0 electrodes at 10C for the mass loadings of 1, 6, and 11 mg·cm^{-2}. (h) Comparison of the rate performance between 1C and 100C for Nb_2O_5/G (solid) and Nb_2O_5/HGF-2.0 (open) electrodes under different mass loadings. (i) The comparison of areal performance metrics of Nb_2O_5/HGF-2.0 electrodes with various commercial and research anodes.

By tailoring the porous structures of electrodes, the charge transport capability of 3D porous HGF composite (*e.g.,* Nb_2O_5/HGF-2.0) with in-plane nanopores can be substantially improved in the comparison of the Nb_2O_5/G composite with a randomly stacked graphene network (Fig. 10e). For the non-3D Nb_2O_5/G electrodes, it is apparent that the mass loading can dramatically increase the overpotential and thus lower the capacity (Fig. 10f), while the optimized Nb_2O_5/HGF-2.0 electrode show a much smaller overpotential (less internal resistance) and capacity loss with increasing mass loading (Fig. 10g). As a result, the Nb_2O_5/HGF-2.0 electrode is optimized to deliver much less capacity degradation induced by mass loading at various C-rates (Fig. 10h). In general, in contrast to the rapid decay in areal capacity with increasing current density observed in a typical commercial or research devices (Fig. 10i), our composite electrode exhibits a much more gradual change. At > 5 mA·cm^{-2}, the optimized Nb_2O_5/ HGF-2.0 electrode delivers a much higher areal capacity at a given current density. Moreover, the composite electrodes continue to provide energy storage at high current density beyond 20 mA·cm^{-2}, at which no other battery material system seems to perform.

5. Three-dimensional graphene membrane cathode for high energy density rechargeable lithium-air batteries in ambient conditions

Lithium-air (Li-air) batteries with aprotic electrolytes have attracted intense interest for use in mobile energy supplies because of their potential to offer energy densities far exceeding those of lithium-ion batteries and other energy storage systems. Compared to most studies focusing on Li-air batteries operated in pure oxygen, the operation of Li-air batteries in ambient air is more relevant to practical applications and is considerably more challenging. However, the low oxygen partial pressure in air can limit the ability of O_2 to access the cathode. For this reason, it is desirable to have a cathode that is highly porous for fast oxygen diffusion, and also with a high specific surface area for efficient charge/discharge cycles. In addition, the moisture in the ambient air can react with the discharge product (Li_2O_2) and/or even corrode the Li anode, sabotaging the battery's inner systems and severely undermining its stability and cycling endurance.

Graphene, a single atomic layer of a graphite sheet, has recently been explored as a Li-air battery electrode due to its excellent electrical conductivity and high surface area. Additionally, it has been suggested that the defects and functional groups on the reduced graphene oxide can function as catalytic active sites for both oxygen evolution reactions (OER) and oxygen reduction reactions (ORR) that are essential for charge/ discharge processes. By using densely packed three-dimensional (3D) graphene membrane as an effective cathode, we can create a binder-free and hydrophobic system for the stable and reversible operation of Li-air batteries under ambient conditions.

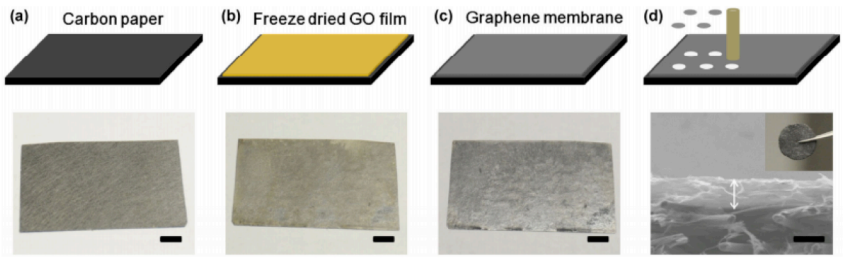

Fig.11. An illustration of the scalable preparation of the 3D graphene membrane cathode. (a) Commercial carbon paper is used as the support. (b) Graphene oxide is coated on the carbon paper. (c) A graphene membrane is formed after annealing. (d) The membrane is cut into round disks for coin cell assembly and a cross sectional SEM image of the graphene membrane cathode is recorded. Scale bars are 1 cm in (a)–(c), and 20 μm in (d).

The 3D graphene membrane exhibits several unique characteristics, making it an excellent air cathode material. First, the 3D graphene membrane consists of a highly conjugated and interlocked 3D network structure of graphene sheets, and it is mechanically strong alone as a binder-free air-cathode. This prevents structural/chemical instability and reduces the mass of passive components. Secondly, the highly interconnected 3D graphene network structure can ensure excellent electron transport properties across the entire network. Thirdly, the highly porous network of channels within the 3D graphene membrane can offer highly efficient diffusion pathways for oxygen and electrolyte ions. Moreover, the high specific surface area of a porous graphene network with abundant defects can offer many active sites for ORR and OER, which support efficient charge/discharge processes. The 3D graphene skeleton structure can also allow high capacity deposition of the insulating discharge product Li_2O_2 while maintaining the overall structural and electronic integrity and stability in a deep discharge state. Finally, the highly tortuous, hydrophobic and densely packed architecture can offer important O_2/H_2O

selectivity to ensure efficient oxygen diffusion while retarding the ingression of moisture. This minimizes the adverse impact of moisture under ambient conditions. Together, these unique attributes of the proposed graphene membrane cathode can enable a high capacity Li-air battery with stable cycling performance in both oxygen and ambient conditions. Commercially available carbon paper was used as the support for the 3D graphene membrane cathodes. Fig. 11a-d show the schematic diagrams and SEM images of our electrode preparation process. The thickness and density of the graphene membrane can be readily tuned to support stability, energy and power requirements.

To evaluate the cycling stability of our Li-air batteries under ambient conditions, we have cycled the devices at different charge/discharge capacities. The Li-air battery is first cycled with a moderate capacity of 1,425 mAh/g (Fig. 12a). Interestingly, the device displays highly stable cycling behavior for up to 100 cycles, nearly the same charge/discharge behavior during each cycle (Fig. 12b). After 50 cycles, the charge overpotential begins to gradually increase and reaches 3.8 V at 100 cycles.

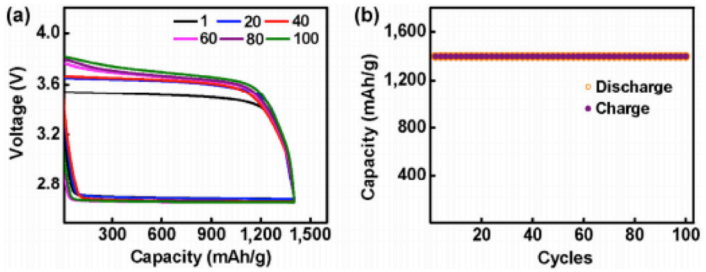

Fig. 12. Capacity-limited cycling test. (a) Galvanostatic cycling of a Li-air cell with a 3D graphene membrane cathode at a capacity of ~ 1,425 mAh/g. (b) Cycling profiles at a capacity of ~ 1,425 mAh/g in ambient air. Current rate is 2.8 A/g.

In summary, our studies demonstrate that a binder-free, high-capacity air cathode can be constructed using a dense, hydrophobic 3D graphene membrane. The 3D graphene membrane structure has a highly interconnected graphene network for efficient charge transport, a highly porous structure for efficient diffusion of oxygen and electrolyte ions, and a large specific surface area for high-capacity storage of the discharge product, Li_2O_2. Finally, the highly tortuous hydrophobic graphene membrane generates O_2/H_2O selectivity and effectively retards moisture diffusion to ensure excellent charge/discharge cycling performance under ambient conditions. Together, these combined features allow us to create a Li-air battery with excellent cycling performance (> 2,000 cycles with 140 mAh/g and > 100 cycles with 1,425 mAh/g) and an extremely high capacity (> 5,700 mAh/g over 20 cycles). Our results demonstrate that a scalable, high-capacity and long life-cycle Li-air battery cathode can be achieved by rationally designing a graphene moisture-resistive membrane cathode.

6. Surface engineering of ultrafine platinum nanowires enable record-high mass activity for oxygen reduction reaction

To overcome the sluggish kinetics of oxygen reduction reaction (ORR) in fuel cell application, platinum (Pt) was widely recognized as the most active element for ORR. However, the extreme scarcity and high of Pt represent a key obstacle towards wide spread application of fuel cells. Therefore, To reduce the required platinum usage requires to improve the Pt mass activity. The Pt mass activity is mainly determined by the specific activity (SA) and the electrochemically active surface area (ECSA). In this case, to boost Pt mass activity, an ideal catalyst should have an ORR favorable chemical environment for high specific activity, optimized geometric factors for high ECSA and a mechanism to maintain these high values for long periods of operation.

To this end, we have recently developed a unique ultrafine jagged Pt nanowires (J-PtNWs) with rich ORR-favorable rhombic configurations showing a specific activity of 11.5mA/cm^2 at 0.9 V versus RHE and a record high ECSA of 118 m_2/g_{Pt}. Together, these J-PtNWs deliver a mass activity of 13.6 A/mg_{Pt} (at 0.9 V versus RHE), which is ~ 50 times that of the state-of-the-art commercial Pt/C catalyst. Fig. 13 shows a schematic diagram of the synthetic route to produce J-PtNWs. Firstly, we synthesized the Pt@NiO core-shell nanowires, with a typical overall diameter of ~ 5 nm or less, and a length of ~ 250 nm-300 nm (Fig. 13a). The as-synthesized core-shell NWs were then loaded on carbon black, and annealed under Ar/H_2 (97:3) atmosphere at 450 ºC for 12 hours to form PtNi alloy NWs (Fig. 13b). Lastly, an electrochemical leaching process was used to leach out all the Ni atoms, leaving a defective surface on the remaining ultrafine platinum nanowires (Fig. 13c).

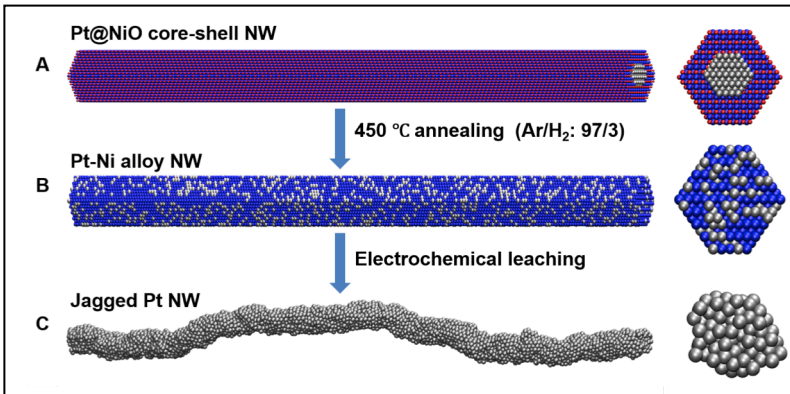

Fig. 13. An illustration diagram of (a) Pt@NiO core-shell nanowire, (b) Pt-Ni alloy nanowire annealed at 450 °C for 12 hours, (c) Jagged platinum nanowire after electro-chemical de-alloy process.

The electrochemical dealloying (leaching) process was performed via cyclic voltammetry (CV) in N_2-saturated 0.1 M $HClO_4$ solution (0.05 V to 1.10 V versus RHE) with a sweep rate of 100 mV·s^{-1} (Fig.14a). With the CV curves, the $ECSA_{Hupd}$ was derived from the Hupd adsorption/desorption peak areas (0.05 V < E < 0.35 V) normalized by the total mass of the loaded Pt. The PtNi alloy nanowires initially showed an essentially negligible $ECSA_{Hupd}$ during the first CV cycle. The $ECSA_{Hupd}$ increased steadily with the increasing number of CV cycles (Fig. 14b). The nanowires were fully activated in ~ 160 CV cycles to reach a stable $ECSA_{Hupd}$ up to 118 m^2/g_{Pt}, whereas the previous highest reported values were ~ 70 m^2/g_{Pt}. We used CV to measure the ECSA (Fig. 14c). Overall, the J-PtNWs, R-PtNWs and Pt/C catalyst showed ECSA values of 118, 110 and 74 m^2/g_{Pt}, respectively (Pt mass loading on electrode: 2.2 mg/cm^2 for Jagged PtNWs, 2.55 mg/cm^2 for Regular PtNWs, and 7.65 mg/cm^2 for Pt/C catalyst).

Fig. 14d shows the ORR polarization curves normalized by glassy carbon electrode geometric area (0.196 cm^2). The half-wave potential for the J-PtNWs was 0.935 V, which is considerably higher than those of the commercial Pt/C catalyst (0.86 V) and the R-PtNWs (0.90 V), suggesting excellent ORR activity of the J-PtNWs. The Koutecky-Levich equation was used to calculate the kinetic current by considering the mass-transport correction. The specific and mass activities were normalized by the ECSA or the total mass of the loaded Pt, respectively. Overall, the J-PtNWs showed a specific activity of 11.5 mA·cm^{-2} at 0.90 V versus RHE, far higher than 0.35 mA/cm^2 for the Pt/C catalyst or 1.59 mA·cm^{-2} for the R-PtNWs tested under the same conditions. Together with their ultra-high specific surface area, the J-PtNWs deliver a high mass activity of 13.6 A/mg_{Pt} at 0.9 V versus RHE, which is 52 times that of the 10 weight percent Pt/C (0.26 A/mg_{Pt}), and more than 7 times that of the R-PtNWs (1.76 A/mg_{Pt}). Fig. 14g shows that J-PtNWs still exhibited a mass activity 48 times than that of the Pt/C catalyst. The Tafel plots of specific activity (Fig. 14e) exhibit slopes of 51, 72, and 74 mV·decade^{-1} for the J-PtNWs, R-PtNWs, and Pt/C catalyst, respectively. A considerably smaller slope achieved in the J-PtNWs suggests significantly improved kinetics for ORR. Remarkably, the mass activity Tafel plot (Fig. 14f) shows that the J-PtNWs deliver mass activity 30 times than the 2017 target set by the U.S. Department of Energy (DOE) (0.44 A/mg_{Pt} at 0.90 V for MEA, highlighted by purple

dashed line in Fig. 14f). The J-PtNWs can deliver the DOE targeted mass activity at 0.975 V (RHE), thus reducing the overpotential by 0.075 V.

We evaluated the durability of the J-PtNWs using accelerated deterioration tests (ADT) under a sweep rate of 100 $mV \cdot s^{-1}$ between 0.6 V and 1.0 V in O_2 saturated 0.1 M $HClO_4$. After 6000 cycles, the ECSA dropped by only ~ 7%, the specific activity dropped by only ~ 5.5%, and together the mass activity dropped by only 12% (Fig. 14h). The retention of high ECSA in J-PtNWs during ADT is in stark contrast to that of the Pt/C catalyst, and high-resolution STEM studies showed that the jagged surface (with defective sites) was largely preserved after 6000 cycles (Fig. 14i).

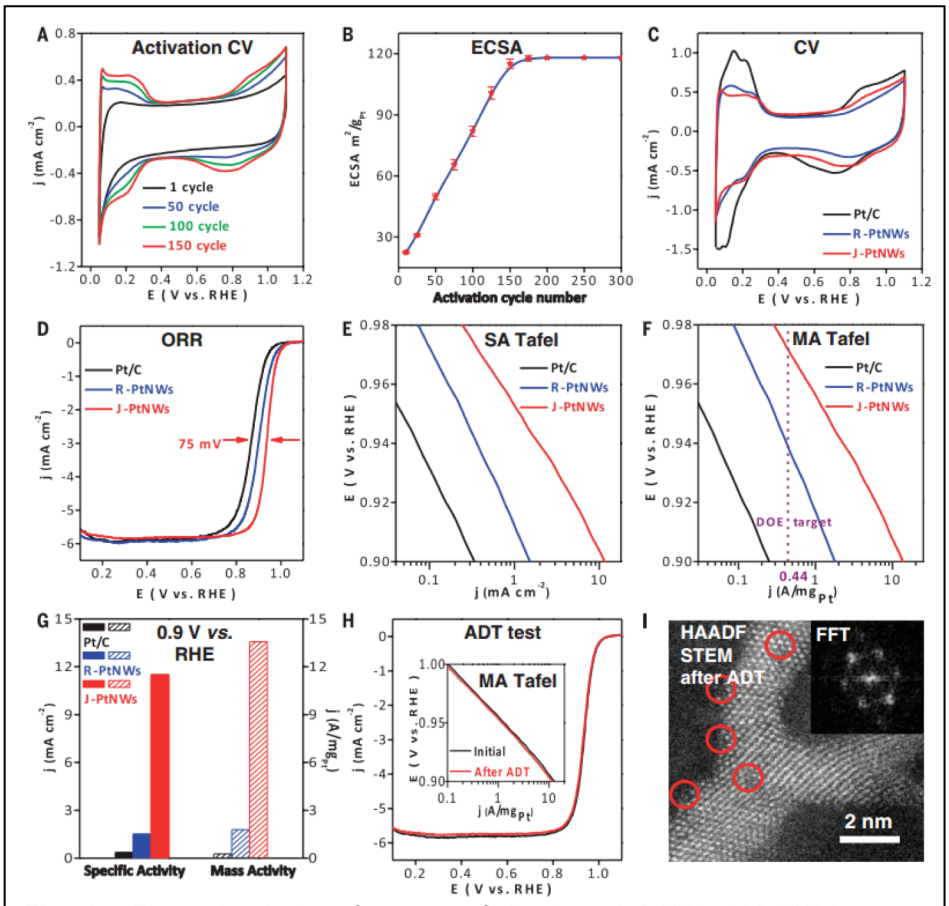

Fig. 14. Electrochemical performance of the jagged PtNWs (J-PtNWs) versus regular synthetic PtNWs (R-PtNWs) and commercial Pt/C catalyst. (a) Cyclic voltammetry (CV) curves corresponding to different activation cycles of the dealloying process, clearly indicating the increasing surface area with increasing number of CV cycles. (b) The evolution of ECSA with increasing number of CV cycles, showing that 160 cycles are sufficient to construct the J-PtNW and reach a stable ECSA. (c and d) CV and ORR polarization curves for the J-PtNWs, R-PtNWs, and Pt/C catalyst, respectively. (e and f) Specific activity (SA) and mass activity (MA) Tafel plot for the J-PtNWs, R-PtNWs, and Pt/C catalyst, respectively. The purple dashed line indicates the 2017 mass activity target (at 0.90 V versus RHE) set by DOE. (g) Comparison of specific activities and mass activities of the J-PtNWs, R-PtNWs, and Pt/C catalyst at 0.9 V versus RHE, showing that the J-PtNWs deliver 33 times the specific activity or 52 times the mass activity of the Pt/C catalyst. (h) ORR polarization curves and mass activity Tafel plot (inset) for the J-PtNWs before and after 6000 CV cycles between 0.6 and 1.0 V versus RHE, showing little loss in activity. The scan rate for the accelerated durability test (ADT) is 100 mV s^{-1}. (i) High-resolution HAADF-STEM image of the J-PtNWs after ADT. The circled areas indicate defective regions with missing atoms. The inset shows the corresponding FFT image.

Further simulation and EXAFS result also confirmed that such de-alloying process will lead to a 1.8% shorter first-shell Pt-Pt bond length in the J-PtNWs (2.71 Å) than that of the Pt foil (2.76 Å). This mechanical strain can decrease the binding energy of adsorbents on close-packed platinum surfaces and hence boost the ORR property.

7. Composition tunable ternary Pt-Ni-Co octahedra for optimized oxygen reduction activity

Pt-based catalysts have been the best candidates so far serving the current needs of the ORR for high activity and stability. However, the high cost and relative scarcity of Pt limit the cost-efficiency of automobile fuel cells. Tuning the composition and exposed facet of platinum-based multi-metallic nanocrystals opens vast possibilities for enhancing the ORR performance.

By using an effective one-step method enabling the synthesis of Pt-Ni-Co octahedra with tunable compositions, which subsequently allows us to optimize ORR activity through fine composition modulation. We first synthesized three Pt-Ni-Co octahedral with composition of Pt : Ni : Co = 1 : 0.9 : 0.05, 1 : 0.6 : 0.05, 1 : 0.4 : 0.05, 1 : 0.55 : 0.1, and 1 : 0.5 : 0.15, respectively. The XRD peaks showed a considerable shift corresponding to the change in Pt composition in the alloy (Fig. 15a and 15b). Fig. 15c shows a uniform dispersed on carbon black, and the Fig. 15d showed a {111} inter-planar distance of 0.218 nm for $PtNi_{0.55}Co_{0.1}$/C. EDS mapping of an octahedron from $PtNi_{0.55}Co_{0.1}$/C was also shown in Fig. 15e.

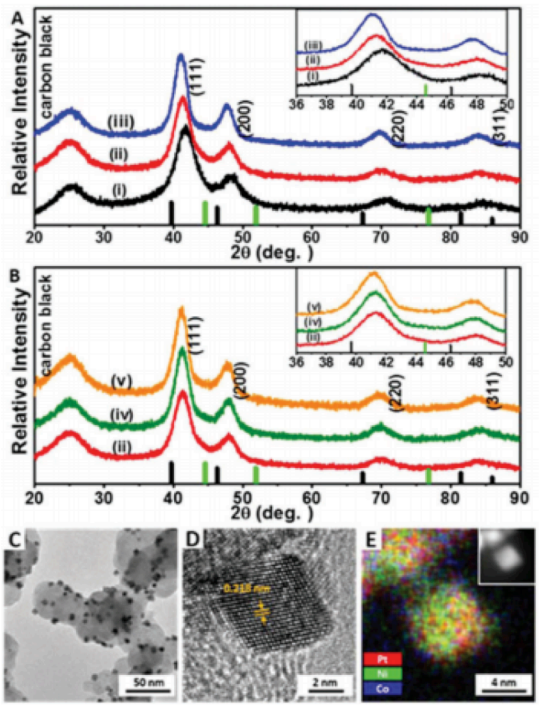

Fig. 15. (a) XRD spectra of octahedral samples (i) $PtNi_{0.9}Co_{0.05}$/C, (ii) $PtNi_{0.6}Co_{0.05}$/C, and (iii) $PtNi_{0.4}Co_{0.05}$/C, inset: zoom in of the XRD spectra; black and green perpendicular lines represent the positions of standard Pt and Ni peaks, respectively. (b) XRD spectra of octahedral samples (ii) $PtNi_{0.6}Co_{0.05}$, (iv) $PtNi_{0.55}Co_{0.1}$, and (v) $PtNi_{0.5}Co_{0.15}$, inset: zoom in of the XRD spectra; black and green perpendicular lines represent the positions of standard Pt and Ni peaks, respectively. (c) TEM image and (d) representative HRTEM image of $PtNi_{0.55}Co_{0.1}$/C. (3) EDS mapping of an octahedron from $PtNi_{0.55}Co_{0.1}$/C, inset: the scanning transmission electron microscopy (STEM) image of the same area for EDS mapping.

We compared the activity of our composition optimized octahedral $PtNi_{0.55}Co_{0.1}$/C with commercial Pt/C (20 wt% Pt, Pt particle size: 2-5 nm), and octahedral $PtNi_{0.65}$/C. $PtNi_{0.65}$/C was prepared using a similar method with a comparable size, morphology and Pt ratio to $PtNi_{0.55}Co_{0.1}$/C. The specific activity and mass activity of octahedral $PtNi_{0.55}Co_{0.1}$/C were both about 1.5 times than those of octahedral $PtNi_{0.65}$/C (a specific activity of 3.43 mA/cm^2 and a mass activity of about 1.81A/mg_{Pt}). In addition, octahedral $PtNi_{0.55}Co_{0.1}$/C showed 20.2 times higher specific activity and 14.7 times higher mass activity relative to those of commercial Pt/C, respectively (a specific activity of 0.25 mA/cm^2 and a mass activity of 0.19 A/mg_{Pt}).

In summary, we demonstrated an effective one-step method that allowed the fine-tuning of composition while maintaining the morphology and size of Pt-Ni-Co nanocatalysts. The modification of the Pt:(Ni + Co) ratio with the fixed Pt:Co ratio showed that a Pt:(Ni + Co) ratio of 1:0.65 showed the highest activity among tested samples (i), (ii) and (iii). Furthermore, with a fixed Pt:(Ni + Co) ratio of around 1:0.65, the Ni:Co ratio was tuned to optimize the ORR activity. Sample (iv) with Pt:Ni:Co = 1:0.55:0.1 was found to demonstrate the highest ORR activity among all tested compositions. Ultimately, the composition optimized octahedral $PtNi_{0.55}Co_{0.1}$/C indicated a significant ORR performance improvement compared to octahedral $PtNi_{0.65}$/C, commercial Pt/C and previously reported Pt-Ni-Co alloy octahedra. The strength of the method

is that it offers a pathway to investigate the composition-dependent ORR activity of ternary alloys that can be delineated from other influences.

8. Copper and nitrogen co-doped carbon composites for oxygen reduction reaction

An efficient non-noble metal catalyst for the oxygen reduction reaction (ORR) is of great importance for the fabrication of cost-effective fuel cells. Nitrogen-doped carbons with various transition metal co-dopants have emerged as attractive candidates to replace the expensive platinum catalysts. We prepared several copper- and nitrogen-doped carbon materials as highly efficient ORR catalysts by pyrolyzing porphyrin-based metal-organic frameworks, and investigated the effects of air impurities during the thermal carbonization process. Our results indicate that the introduction of air impurities can significantly improve ORR activity in nitrogen-doped carbon and the addition of copper co-dopant further enhances the ORR activity to exceed that of platinum. Systematic structural characterization and electrochemical studies demonstrate that the air-impurity-treated samples show significantly higher surface area and electron transfer numbers, suggesting that the partial etching of the carbon by air leads to increased porosity and accessibility to highly active ORR sites. Our study represents the first example of using air or oxygen impurities to tailor the ORR activity of metal and nitrogen co-doped carbon materials; hence, opening a new avenue to engineer the catalytic activity of these materials.

We chose MOF-545, with zirconia cluster SBUs and porphyrin linkers to form wirelike crystals to study the effects of Cu-doping and air treatment. Specifically, we prepared four parallel samples containing NC obtained by annealing MOF-545 with metal-free porphyrin linkers (1) in pure argon (NC) (2) and in argon with air impurities (NC-air). On the other hand, Cu-NC was obtained by annealing MOF-545 with copper porphyrin linkers (3) in pure argon (Cu-NC) and (4) in argon with air impurities (Cu-NC-air). The SEM images of the initial MOF crystals (Fig. 16a) and the annealed MOF samples clearly showed that the wire-like morphology was maintained after the annealing process (Fig. 16b,c), which can be readily processed and drop-coated on the rotating disk electrode for electrochemical studies. For the electrochemical characterization, a rotating disk electrode was used, equipped with a Pt counter electrode and a saturated calomel reference electrode. The cyclic voltammetry (CV) curves of the pure argon annealed samples NC and Cu-NC exhibit a rather broad and moderate peak around 0.7 V vs RHE (blue lines in Figure 17d and Fig. 16e), suggesting apparent ORR activity. The ORR activity of these pure Ar annealed samples was further confirmed by the linear sweep voltammetry (LSV) curves (blue lines in Fig. 16f and Fig. 16g), although with considerably lower performance compared to platinum on carbon (Pt/C) (black line). From electrochemical test results of our four different nitrogen-doped carbon, we initially noticed that

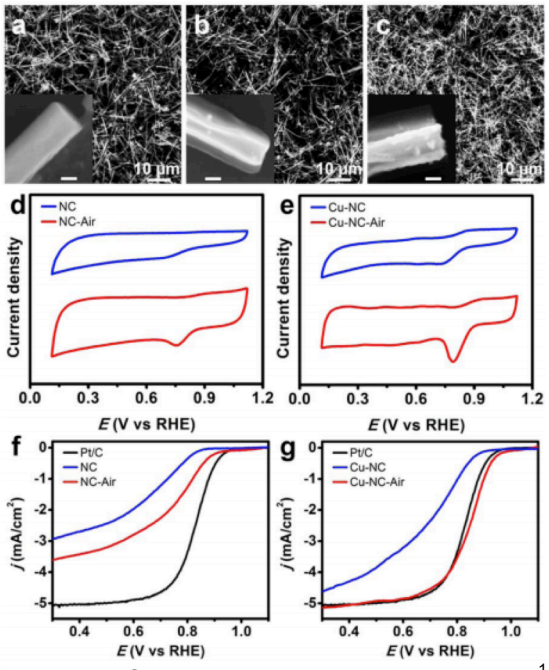

Fig. 16. (a) CV curves were recorded at 100 $mV \cdot s^{-1}$ from 0.05 to 1.1 V vs. RHE in N_2 saturated 0.1 M $HClO_4$. (b) ORR polarization curves were recorded at 1600 rpm from 0.05 to 1.1 vs. RHE in O_2 saturated 0.1 M $HClO_4$. (c) Comparison of ORR specific and mass activities of octahedral $PtNi_{0.65}/C$, octahedral $PtNi_{0.55}Co_{0.1}/C$, and Pt/C, respectively.

both NC and Cu-NC frameworks showed relatively low activity; after air treatment, however, a considerable improvement in the ORR activity was observed. Our studies suggest that the increase in ORR activity can be attributed to an increase in electrochemical surface area and a highly porous structure, leading to the accessibility of new active sites. The air treatment method described in this work can be applied to enhance the performance of carbon-based materials in a multitude of applications requiring high surface area and porosity.

9. Molecular ligand modulation enable robust oxidation property of cyclohexenone to phenol on palladium heterogeneous nanocatalysts

Heterogeneous nanoparticle catalysts are a topic of increasing interest due to their long-term stability, recyclability and easier separation from the reaction mixture. Molecular ligands play an essential role in the design of homogeneous molecular catalysts, where the molecular ligands can be used to tune the catalytic activity, selectivity, versatility and stability. On the other hand, the impact of molecular ligands on nanoparticle catalysts is far less understood. To date, most efforts have been limited to exploring the roles of molecular ligands in controlling the size and the facet of nanoparticles during nanoparticle synthetic steps.

Aerobic oxidation reactions have attracted significant industrial attention because of their mild and green conditions. Homogenous Pd catalysts have proved successful in driving these reactions. However, the inevitable degradation processes during the aerobic oxidation cycles can lead to the formation of inactive Pd black and deactivate the catalysts (Fig. 17). Phenols are recognized as the key structural motif and core building block for a wide range of industrial chemicals. The selective functionalization of phenols is generally challenging.

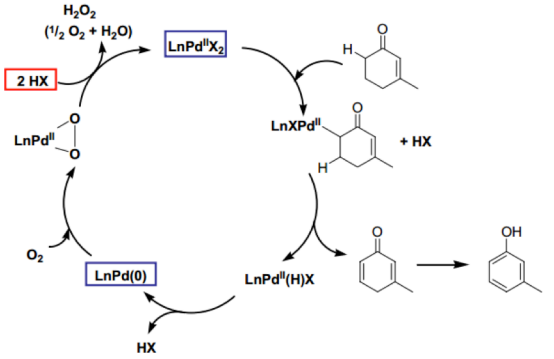

Fig. 17. Reaction pathway of Pd-catalyzed aerobic dehydrogenative oxidation of cyclohexenone to phenol. Ln represents the various b-substituted butyric acid ligands. HX represents the acids added to the reaction.

For catalysts synthesis, we used butyric acid with variable b-substitution as the secondary binding site to engineer the particle stability. Instead of engineering the primary binding functional group that could fundamentally change the nanoparticle size/morphology or directly passivate the catalytic active sites, the b-functional groups can function as secondary binding sites to capture/retain the leached Pd(II) ions near the nanoparticle surface, and regulate their participation in the catalytic cycle without significantly altering the binding conditions to the nanoparticle surfaces. The Pd nanoparticles were synthesized with a diameter of 10 nm using HB as the capping agent. The particle synthesis was conducted in aqueous solutions containing Na_2PdCl_4, ascorbic acid and $NaBH_4$. Fourier transforms infrared (FT-IR) studies confirm that the carboxylic group strongly binds to the Pd surfaces, whereas the β-hydroxyl group only weakly interacts with the Pd surfaces.

The resulting nanoparticles were supported on carbon black and used as the catalysts [3-hydroxybutyric acid–ligated Pd nanoparticles (HB-Pd/C)] for aerobic oxidation of cyclohexenone to phenol, which is compared with the catalytic behavior of the homogeneous catalyst $Pd(TFA)_2$.

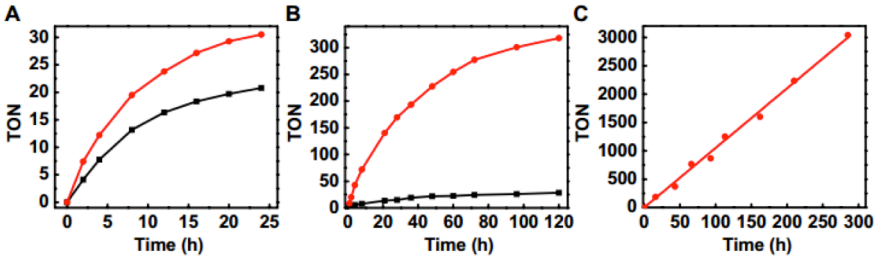

Fig. 18. Comparison of TON of heterogeneous nanoparticle catalysts with homogeneous molecular catalysts. TON of time-dependent reaction catalyzed by HB-Pd/C (red line) and $Pd(TFA)_2$ (black line) with different substrate/catalyst ratios of (a) 100:3, (b) 1000:3, and (c) 10,000:3.

Under the reaction conditions of various substrate/catalyst ratios, the TON normalized by the total amount of Pd catalyst has been determined. TON is an important measure of catalyst stability. Under low turnover conditions, namely low substrate/catalyst ratio (100:3), the TON of the heterogeneous nanoparticle catalyst HB-Pd/C is 31, about 1.5 times higher than that of the homogeneous $Pd(TFA)_2$ catalyst after a 24-hour reaction (Fig. 18a). With an increased substrate/catalyst ratio of 1000:3 (Fig. 18b), the reaction with the homogeneous $Pd(TFA)_2$ catalysts quickly saturates with a maximum yield of 8.4% and a TON of 28, indicating the deactivation of the catalyst at a low TON. In contrast, with a proper ligand environment, HB-Pd/C could drive the reaction to near completion with a yield of 95.4% and a TON of 314. When we further increase the substrate/catalyst ratio to 10,000:3 (Fig. 18c), the reaction with HB-Pd/C exhibits a linear time course with an unsaturated TON >3000 toward the end of the reaction. These studies clearly demonstrate that the exceptional catalytic activity and stability of HB-Pd/C are largely retained throughout the reaction process.

10. Acknowledgment

I sincerely appreciate a large number of students and postdoctoral researchers who contributed to this research over the past 5 years, including: Xing Zhong, Anxiang Yin, Gongming Wang, Hailong Zhou, Benjamin J. Papandrea, Mohammad Zarghami, Mufan Li, Dehui Li, Boris Volosskiy, Yiliu Wang and collaborators, Prof. Yu Huang, Prof. Williams Goddard, and Prof. Bruce Dunn.

11. A list of papers (mark as published, in press, or submitted) in which DOE support is acknowledged. Include the full text of the acknowledgment section as published.

1. Y. Qu and X. Duan. Progress, challenge and perspective of heterogeneous photocatalysts. *Chem. Soc. Rev.* **42**, 2568-2580 (2013).

"**Acknowledgement.** X.D. acknowledges the support from the U.S. Department of Energy, Office of Basic Energy Sciences, Division of Materials Science and Engineering through Award **DE-SC0008055**. Y.Q. also thanks the partial support from the Ministry of Science and Technology of China through a 973-program under Grant No. 2012CB19401."

2. H. Zhang, X. Zhong, J. C. Shaw, L. Liu, Y. Huang and X. Duan. Very high energy density silicide-air primary batteries. *Energy Environ. Sci.* **6**, 2621-2625 (2013).

"**Acknowledgement.** We acknowledge the support from the U.S. Department of Energy, Office of Basic Energy Sciences, Division of Materials Science and Engineering through Award **DE-SC0008055**."

3. L. Ruan, H. Dakhel, C. Lee, Y. Li, X. Duan, H. Heinz and Y. Huang. A rational biomimetic approach to structure defect generation in colloidal nanocrystals. *ACS Nano* **8**, 6934-6944 (2014).

"**Acknowledgement.** L. Ruan, Y. Li, and Y. Huang acknowledge support from the Office of Naval Research (ONR) (Award N00014-08-1-0985), the Army Research Office (ARO) (Award 54709-MSPCS) and the Sloan Research Fellowship. X.D. acknowledges the support from the U.S. Department of Energy, Office of Basic Energy Sciences, Division of Materials Science and Engineering through Award **DE-SC0008055**. L. Ruan, C. Lee, X. Duan, and Y. Huang also acknowledge the Electron Imaging Center of Nanomachines for TEM and HRTEM support and UCLA Molecular Instrumentation Center for NMR and mass spectroscopy support. H. Ramezani-Dakhel and H. Heinz acknowledge support from the National Science Foundation (Award DMR 0955071), the Air Force Research Laboratory (AFRL and UES, Inc.), and the University of Akron. H. Ramezani-Dakhel and H. Heinz also acknowledge the allocation of computing resources at the Ohio Supercomputing Center."

4. X. Huang, Z. Zhao, Y. Chen, C. Chiu, L. Ruan, Y. Liu, M. Li, X. Duan and Y. Huang. High density catalytic hot spots in ultrafine wavy nanowires. *Nano Lett.* 14, 3887-3894 (2014).

   "**Acknowledgment.** We acknowledge the support from ARO through Award No. 54709-MS-PCS and the ONR under Award N00014-08-1-0985. We thank Electron Imaging Center of Nanomachines at CNSI for the TEM support. Y.H. acknowledges the support from Sloan Research Fellowship. X.D. acknowledges the support from the U.S. Department of Energy, Office of Basic Energy Sciences, Division of Materials Science and Engineering through Award **DE-SC0008055**."

5. B. Volosskiy, K. Niwa, Y. Chen, Z. Zhao, N. O. Weiss, X. Zhong, M. Ding, C. Lee, Y. Huang and X. Duan. Metal-organic framework templated synthesis of ultrathin, well-aligned metallic nanowires. *ACS Nano* **9**, 3044-3049 (2015).

   "**Acknowledgement.** We acknowledge the support from the U.S. Department of Energy, Office of Basic Energy Sciences, Division of Materials Science and Engineering, through Award **DE-SC0008055**. We thank N. Bodzin for his support in making FIB cross sections. We thank EICN at CNSI for the TEM support."

6. Z. Zhao, X. Huang, M. Li, G. Wang, C. Lee, E. Zhu, X. Duan and Y. Huang. Synthesis of stable shape-controlled catalytically active β-palladium hydride. *J. Am. Chem. Soc.* **137**, 15672-15675 (2015).

   "**Acknowledgment.** We acknowledge the support from National Science Foundation (NSF) through award no. DMR-1437263. X.D. acknowledges the support from the U.S. Department of Energy, Office of Basic Energy Sciences, Division of Materials Science and Engineering through Award **DE-SC0008055**. We also thank Electron Imaging Center of Nanomachines at CNSI for the TEM support."

7. G. Wang, D. Li, H. Cheng, Y. Li, C. Chen, A. Yin, Z. Zhao, Z. Lin, H. Wu, Q. He, M. Ding, Y. Liu, Y. Huang and X. Duan. Wafer-scale growth of perovskite single crystal arrays for functional electronics and optoelectronics. *Sci. Adv.* **1**, e1500613 (2015).

   "**Acknowledgment.** We acknowledge the support of the Electron Imaging Center for Nanomachines at University of California Los Angeles, which was funded by the NIH-National Center for Research Resources (grant CJX1-443835-WS-29646) and the NSF Major Research Instrumentation Program (grant CHE-0722519). We also acknowledge the Nanoelectronics Research Facility for providing technical support. X.D. was supported by the U.S. Department of Energy, Office of Basic Energy Sciences, Division of Materials Science and Engineering (award **DE-SC0008055**). Y.H. was supported by the NSF (grant EFRI-1433541)."

8. G. Wang, X. Xiao, W. Li, Z. Lin, Z. Zhao, C. Chen, C. Wang, Y. Li, X. Huang, L. Miao, C.

Jiang, Y. Huang and X. Duan. Significantly enhanced visible light photoelectrochemical activity in TiO_2 nanowire arrays by nitrogen implantation. *Nano Lett.* 15, 4692-4698 (2015).

"**Acknowledgment.** We acknowledge the support from the U.S. Department of Energy, Office of Basic Energy Sciences, Division of Materials Science and Engineering through Award **DE-SC0008055**. We acknowledge Electron Imaging Center for Nanomachines (EICN) at UCLA for the support of TEM, supported with funding from NIH-NCRR Shared Resources Grant (CJX1-443835-WS-29646) and NSF Major Research Instrumentation Grant (CHE-0722519). X.H.X. also acknowledges the support from NSFC (U1260102, 51371131) and NCET (12-0418)."

9. X. Zhong, G. Wang, B. Papandrea, M. Li, Y. Xu, Y. Chen, C.-Y. Chen, H. Zhou, T. Xue, Y. Li, D. Li, Y. Huang and X. Duan. Reduced graphene oxide/silicon nanowire heterostructures with enhanced photoactivity and superior photoelectrochemical stability. *Nano Res.* **8**, 2850-2858 (2015).

   "**Acknowledgment.** We acknowledge the support from the U.S. Department of Energy, Office of Basic Energy Sciences, Division of Materials Science and Engineering through Award **DE-SC0008055**. We acknowledge Electron Imaging Center for Nanomachines (EICN) at UCLA for the support of TEM, supported with funding from NIH- NCRR shared resources Grant (No. CJX1-443835-WS- 29646) and NSF Major Research Instrumentation Grant (No. CHE-0722519)."

10. X. Huang, Z. Zhao, L. Cao, Y. Chen, E. Zhu, Z. Lin, M. Li, A. Yan, A. Zettl, Y. Wang, X. Duan, T. Mueller and Y. Huang. High performance for the oxygen reduction reaction with transition-metal-doped Pt_3Ni octahedra. *Science* **348**, 1230-1234 (2015).

    "Acknowledgement. We acknowledge support from the National Science Foundation (NSF) through award DMR-1437263 on catalysis studies and the Office of Naval Research (ONR) under award N00014-15-1-2146 for synthesis efforts. Computational studies were supported by the NSF through award DMR-1352373 and using computational resources provided by Extreme Science and Engineering Development Environment (XSEDE) through awards DMR130056 and DMR140068. Atomic-scale structural images were generated by using VESTA (*38*). We thank the Director, Office of Energy Research, Office of Basic Energy Sciences, Materials Sciences and Engineering Division, of the U.S. Department of Energy under contract DE-AC02-05CH11231, under the sp^2-bonded materials program, for TEM analytical measurements performed at the National Center for Electron Microscopy at the Lawrence Berkeley National Laboratory. X.D. acknowledges support from the U.S. Department of Energy, Office of Basic Energy Sciences, Division of Materials Science and Engineering through award **DE-SC0008055**. The work at LLNL was performed under the auspices of the U.S. Department of Energy under contract DE-AC52-07NA27344. A.Y. and A.Z. received additional support from NSF grant EEC-083219 within the Center of Integrated Nanomechanical Systems. We also thank the Electron Imaging Center of Nanomachines at CNSI for TEM support."

11. D. Li, G. Wang, H. Cheng, C. Chen, H. Wu, Y. Liu, Y. Huang and X. Duan. Size-dependent phase transition in methylammonium lead iodide perovskite microplate crystals. *Nat. Commun.* **7**, 11330 (2016).

    "**Acknowledgment.** We acknowledge the support from the U.S. Department of Energy, Office of Basic Energy Sciences, Division of Materials Science and Engineering through Award **DE-SC0008055**."

12. H.-C Cheng, G. Wang, D. Li, Q. He, A. Yin, Y. Liu, H. Wu, M. Ding, Y. Huang and X. Duan. Van der waals heterojunction devices based on organohalide perovskites and two-

dimensional materials. *Nano Lett.* **16**, 367-373 (2016).

"**Acknowledgment.** We acknowledge the support from the U.S. Department of Energy, Office of Basic Energy Sciences, Division of Materials Science and Engineering through Award **DE-SC0008055** (material growth) and Office of Naval Research Award N00014-15-1-2368 (device fabrication and characterization)."

13. D. Li, H. Wu, H.-C. Cheng, G. Wang, Y. Huang and X. Duan. Electronic and ionic transport dynamics in organolead halide perovskites. *ACS Nano* **10**, 6933-6941 (2016).

    "**Acknowledgment.** We acknowledge the support from the U.S. Department of Energy, Office of Basic Energy Sciences, Division of Materials Science and Engineering through award **DE-SC0008055**."

14. Z. Zhao, M. Feng, J. Zhou, Z. Liu, M. Li, Z. Fan, O. Tsen, J. Miao, X. Duan and Y. Huang. Composition tunable ternary Pt-Ni-Co octahedra for optimized oxygen reduction activity. *Chem. Commun.* **52**, 11215-11218 (2016).

    "**Acknowledgment.** We acknowledge the support from the National Science Foundation (NSF) through award no. DMR-1437263 for catalytic studies and the Office of Naval Research (ONR) under award N00014-15-1-2146 for synthetic efforts. X. D. acknowledges the support from the U.S. Department of Energy, Office of Basic Energy Sciences, Division of Materials Science and Engineering, through Award **DE-SC0008055**. We also thank the Electron Imaging Center of Nanomachines at CNSI for the TEM support."

15. B. Volosskiy, H. Fei, Z. Zhao, S. Lee, M. Li, Z. Lin, B. Papandrea, C. Wang, Y. Huang and X. Duan. Tuning the catalytic activity of a metal-organic framework derived copper and nitrogen co-doped carbon composite for oxygen reduction reaction. *ACS Appl. Mater. Interfaces* **8**, 26769-26774 (2016).

    "**Acknowledgment.** We acknowledge the support from the U.S. Department of Energy, Office of Basic Energy Sciences, Division of Materials Science and Engineering through Award **DE-SC0008055**. Y.H. acknowledges the support from the National Science Foundation (NSF) through Award DMR-1437263 (electrochemical characterization)."

16. M. Li, Z. Zhao, T. Cheng, A. Fortunelli, C. Chen, R. Yu, Q. Zhang, L. Gu, B. Merinov, Z. Lin, E. Zhu, T. Yu, Q. Jia, J. Guo, L. Zhang, W. Goddard, Y. Huang and X. Duan. Ultrafine jagged platinum nanowires enable ultrahigh mass activity for the oxygen reduction reaction. *Science* **354**,1414-1419 (2016).

    "**Acknowledgment.** We acknowledge the support from the U.S. Department of Energy, Office of Basic Energy Sciences, Division of Materials Science and Engineering through Award **DE-SC0008055** (synthesis and structural analysis). Y.H. acknowledges the support from the National Science Foundation through Award DMR-1437263 (electrochemical characterizations). The Advanced Light Source is supported by the Director, Office of Science, Office of Basic Energy Sciences, of the U.S. Department of Energy under Contract No. DE-AC02-05CH11231. We thank Dr. Matthew A. Marcus at ALS for the support during the acquisition of XAS data, and C. Wu for help on EXAFS data analysis. R.Y. acknowledges support from the National Natural Science Foundation of China project number 51525102, 51390475, 51371102. The aberration-corrected transmission electron microscopy results were achieved (in part) using Titan 80-300 and JEM-ARM 200F. In this work, we used the resources of the National Center for Electron Microscopy in Beijing. A patent application on this subject has been filed."

17. D. Li, H. C. Cheng, Y. Wang, Z. Zhao, G. Wang, H. Wu, Q. He, Y. Huang and X. Duan. The effect of thermal annealing on charge transport in organolead halide perovskite microplate

field-effect transistors. *Adv. Mater.* **29**, 1601959 (2017).

"**Acknowledgment.** D.L. and H.-C.C. contributed equally to this work. The authors acknowledge the Nanoelectronics Research Facility (NRF) for technical support. X.D. acknowledges the support from the U.S. Department of Energy, Office of Basic Energy Sciences, Division of Materials Science and Engineering through Award **DE-SC0008055** (materials synthesis and characterization). Y.H. acknowledges the support by National Science Foundation EFRI-1433541 (device characterization)."

18. D. Li, H.-C. Cheng, H. Wu, Y. Wang, J. Guo, G. Wang, Y. Huang and X. Duan. Gate-induced insulator to band-like transport transition in organolead halide perovskite. *J. Phys. Chem. Lett.* **8**, 429-434 (2017).

"**Acknowledgment.** We acknowledge the Nanoelectronics Research Facility (NRF) for technical support. D.L. acknowledges the financial support from National Young 1000-Talent Program and the National Natural Science Foundation of China, Grant No. 61674060. X.D. acknowledges the support from the U.S. Department of Energy, Office of Basic Energy Sciences, Division of Materials Science and Engineering through Award **DE-SC0008055** (material synthesis). Y.H. acknowledges the support from National Science Foundation EFRI-1433541 (device fabrications and characterizations)."

19. X. Zhong, B. Papandrea, Y. Xu, Z. Lin, H. Zhang, Y. Liu, Y. Huang and X. Duan. Three-dimensional graphene membrane cathode for high energy density rechargeable lithium-air batteries in ambient conditions. *Nano Res.* **10**, 472-482 (2017).

"**Acknowledgment.** We acknowledge the support from the U.S. Department of Energy, Office of Basic Energy Sciences, Division of Materials Science and Engineering through Award **DE-SC0008055**. We acknowledge Electron Imaging Center for Nanomachines (EICN) at UCLA for the support of TEM, supported with funding from NIH-NCRR shared resources Grant (No. CJX1-443835-WS-29646) and NSF Major Research Instrumentation Grant (No. CHE-0722519)."

20. T. Xue, Z. Lin, C.-Y. Chiu, Y. Li, L. Ruan, G. Wang, Z. Zhao, C. Lee, X. Duan and Y. Huang. Molecular ligand modulation of palladium nanocatalysts for highly efficient and robust heterogeneous oxidation of cyclohexenone to phenol. *Sci. Adv.* **3**, e1600615 (2017).

"**Acknowledgment.** X.D. acknowledges the support from the U.S. Department of Energy, Office of Basic Energy Sciences, Division of Materials Sciences and Engineering through award **DE-SC0008055** (nanocatalyst characterization and catalytic studies)."

21. Y. Wang, X. Guan, D. Li, H.-C. Cheng, X. Duan, Z. Lin and X. Duan. Chemical vapor deposition growth of single-crystalline cesium lead halide microplatelets and heterostructures for optoelectronic applications. *Nano Res.* **10**, 1223-1233 (2017).

"**Acknowledgment.** We acknowledge the support from the U.S. Department of Energy, Office of Basic Energy Sciences, Division of Materials Science and Engineering through Award **DE-SC0008055.** The effort at Hunan University was supported by National Natural Science Foundation of China (No. 61528403)."

22. H. Sun, L. Mei, J. Liang, Z. Zhao, C. Lee, H. Fei, M. Ding, J. Lau, M. Li, C. Wang, X. Xu, G. Hao, B. Papandrea, I. Shakir, B. Dunn, Y. Huang and X. Duan. Three-dimensional holey-graphene/niobia composite architectures for ultrahigh-rate energy storage. *Science* **356**, 599-604 (2017).

"**Acknowledgment.** H.S., H.F., and I.S. extend sincere appreciation to the Deanship of Scientific Research at King Saud University for its funding of this research through grant PEJP-17-01 (material preparation and electrochemical studies). X.D. and M.L. thank the U.S.

Department of Energy (DOE) Office of Basic Energy Sciences, Division of Materials Science and Engineering, award **DE-SC0008055** (structural characterizations). Y.H. M.D. and Z.Z. appreciate the support from the National Science Foundation through award DMR-1437263 (ion transport studies). B.D. and J.L. greatly appreciate the support by the Office of Naval Research (N00014-16-1-2164) (impedance analysis). L.M., J.L., X.X., and G.H. thank the Chinese Scholar Council scholarship for the financial support (materials preparation of electrochemical studies). L.M. also thanks a postdoctoral fellowship from Hunan University. Holy-graphene/niobia composite are available from the University of California, Los Angeles (UCLA) under a materials transfer agreement with the University. A provisional patent application has been filed by UCLA (UCLA Case 2017-216) that covers the subject described here."